

The Application of Compact Polarization Decomposition in the Construction of a Dual-Polarization Radar Index and the Effect Evaluation of Rape Extraction

Bingkun Liang ¹, Student Member, IEEE, Rongkun Zhao, Jieyang Tan, Lang Xia ², Hong Cao, Shangrong Wu ³, Member, IEEE, and Peng Yang

Abstract—The rape planting plots are fragmented and have the same temporal variation characteristics as other land types, the rape planting area is cloudy and rainy, and the optical remote sensing images are limited, all make it difficult to extract the rape planting areas. Aiming at the above-mentioned problems, this study used microwave remote sensing data combined with the compact polarimetric technique to construct a dual-polarization radar index to classify rape planting areas and analyzed the influence of time series combinations on the extraction accuracy of rape in South China. First, based on $m\text{-}\chi$ compact polarimetric decomposition, a dual-polarization radar vegetation index (RVI) was constructed. Then, based on Sentinel-1 data, the dynamic time warping (DTW) threshold classification method was used to extract rape planting areas in six counties in the main rape-producing areas in the middle and lower reaches of the Yangtze River, China. Finally, a random forest algorithm was used to analyze and screen the optimal time series combination of the extracted regional rape planting areas. Among the 94 rape samples obtained in the field, 74 samples were accurately classified as rape, and the overall accuracy was 78.72%. Six ground samples were used to verify the accuracy of the rape planting area extraction results, and the F-1 score was 81.00%. The above-mentioned results indicated that the rape planting area extraction approach based on the $\text{RVI}_{m\text{-}\chi}$ and DTW threshold classification methods yields high accuracy in regional rape planting

area extraction from dual-polarization SAR data, and $\text{RVI}_{m\text{-}\chi}$ is characterized by certain regional scalability and stability.

Index Terms—Planting area, polarization decomposition, radar vegetation index (RVI), rape, sentinel-1 data.

I. INTRODUCTION

RAPE (*Brassica napus* L.) is one of the most important oil crops in the world, and it is the main source of edible vegetable oil, feed protein, and biological lubricating oil; thus, it has significant economic value in food manufacturing and pharmaceutical industries [1], [2]. China's rape planting area and production are among the highest in the world, providing more than 50% of the oil supply for Chinese residents every year. According to the rape planting area and production data for the past ten years, the annual planting area of rape in China is between 5.5 and 7.5 million hectares, the annual yield is between 1800 and 2100 kg/ha, the annual production of rapeseed is between 10 and 15 million tons, and the overall trend is on the rise (<http://www.stats.gov.cn>). Real-time, dynamic, and large-scale monitoring of rape planting areas is of great significance for guiding agricultural production, maintaining the stability of the grain and oil markets, and ensuring the life and health of the people of China.

The fragmentation of rape planting plots and seasonal changes in other land covers, such as woodland and water, with the same temporal characteristics as rape in single-phase or multiphase remote sensing images make the extraction of rapeseed planting areas difficult. Therefore, there are few studies related to the extraction of rape planting areas using remote sensing technology. Most of the previous studies on rape extraction were based on optical remote sensing data [3], [4], using the optical vegetation index and combining it with the phenological information of rape to construct extraction models. However, the weather in the main rape-producing areas is cloudy and rainy, and the lack of high-quality optical data due to the influence of meteorological conditions such as clouds, rain, and fog, and the fragmentation of rape planting plots have led to great difficulties in monitoring rape planting areas [5], [6]. Synthetic aperture radar (SAR) provides all-day and all-weather observations and is not affected by meteorological conditions; additionally, the

Manuscript received 8 April 2023; revised 28 April 2023; accepted 23 May 2023. Date of publication 5 June 2023; date of current version 16 June 2023. This work was supported in part by the National Key Research and Development Program of China under Grant 2022YFD2001104, in part by the National Natural Science Foundation of China under Grant 42271374, in part by the Fundamental Research Funds for Central Nonprofit Scientific Institutions under Grant 1610132021009, in part by the Youth Innovation Program of Chinese Academy of Agricultural Sciences under Grant Y2023QC18, and in part by the Agricultural Science and Technology Innovation Fund Project of Hunan Province under Grant 2022CX29. (Bingkun Liang and Rongkun Zhao contributed equally to this work.) (Corresponding author: Shangrong Wu.)

Bingkun Liang is with the School of Geography and Planning, Sun Yat-sen University, Guangzhou 510275, China (e-mail: liangbk@mail2.sysu.edu.cn).

Rongkun Zhao, Lang Xia, Hong Cao, Shangrong Wu, and Peng Yang are with the State Key Laboratory of Efficient Utilization of Arid and Semiarid Arable Land in Northern China, Institute of Agricultural Resources and Regional Planning, Chinese Academy of Agricultural Sciences, Beijing 100081, China, and also with the Key Laboratory of Agricultural Remote Sensing, Ministry of Agriculture and Rural Affairs/Institute of Agricultural Resources and Regional Planning, Chinese Academy of Agricultural Sciences, Beijing 100081, China (e-mail: 82101221183@caas.cn; xialang2012@163.com; 82101222095@caas.cn; wushangrong@caas.cn; yangpeng@caas.cn).

Jieyang Tan is with the Institute of Agricultural Economics and Regional Planning, Hunan Academy of Agricultural Sciences, Changsha 410125, China (e-mail: tanjieyang@hunaas.cn).

Digital Object Identifier 10.1109/JSTARS.2023.3283011

side-looking imaging capability of SAR systems makes them sensitive to crops and soil structure and characteristics [7], [8]. In particular, C-band microwave radar signals can reach the crop canopy and are highly sensitive to the 3-D structure of plants [9], [10]. Studies on crop planting area extraction using SAR have focused on grain crops [11], [12], [13], and there are fewer studies related to rape. The current research on rape based on SAR is mainly parameter inversion [5], [14]. Sentinel-1 remote sensing data are currently the only free SAR data (<http://esa-sen4cap.org/>). Sentinel-1 satellites consist of two polar-orbiting satellites in the same orbital plane, and they were successfully launched on April 3, 2014 and April 25, 2016. The satellites are equipped with a C-band SAR system and have four imaging modes, of which the interferometric wide (IW) swath mode acquires data over 250 km at a spatial resolution (single look) of $5 \text{ m} \times 20 \text{ m}$ (range \times azimuth), thus providing a high spatial resolution and large coverage. The Sentinel-1 SAR system covering the main rape-producing areas in the middle and lower reaches of the Yangtze River in China has a revisit period of 12 days and can provide data for the remote sensing-based extraction of rape-planting areas in the region [15].

The characteristics of crop microwave radiation and the interactions between crops and radar microwaves are complex. With the rapid development of radar remote sensing technology, which can now obtain large amounts of data, determining how to extract target crop features from radar remote sensing data has become a key issue in the microwave remote sensing of crops [16], [17], [18]. Polarimetric decomposition technology can effectively obtain the radar polarization characteristics and accurately extract the land cover distribution [19], [20], [21], [22]. Polarimetric decomposition is mainly used in analyses of fully polarized SAR data [23], [24], [25]. Fully polarized data, which contain a variety of information such as horizontal polarization and cross-polarization, have been widely used in crop classification, but there are limitations in terms of data download speed and mapping bandwidth [14]. Therefore, the emergence of compact polarimetric SAR systems has attracted the attention of researchers due to the low design complexity, large imaging range, and strong observation capabilities of these systems [26], [27], [28]. With the development of compact polarization decomposition theory and methods, applied research involving compact polarization is being continuously performed [14], [29], [30], [31], [32]. A compact polarimetric SAR system is essentially a dual-polarization system, and compact polarization decomposition can be applied to dual-polarization SAR data. Although many scholars have studied compact decomposition, there is still a lack of knowledge regarding whether compact polarization decomposition techniques can be applied in crop classification involving dual-polarization radar data. In addition, the radar vegetation index (RVI) reflects the distribution information and growth status of crops [32], [33], which can be used in time series analyses of radar data. At present, the commonly used RVIs mainly include those based on the cross sections of cross-polarization backscattering and copolarization backscattering [34], RVIs obtained using the eigenvalue spectrum obtained from the coherency matrix T [35], and the RVI

based on Freeman polarimetric decomposition and calculated considering volume scattering, dihedral scattering, and surface scattering [36]. However, the data for the above three RVI types need to be decomposed into full-polarization radar data, which is difficult to do in cases with dual-polarization SAR data.

Crops have specific and regular plant characteristics that change with the growth period. Using time series remote sensing images to establish correlations among plants in different phenological stages and specific crop planting areas has always been an important research task and research hotspot in agricultural remote sensing [37], [38], [39]. The key to the classification of land cover based on time series of remote sensing images is to perform similarity analyses of the time series data, that is, to quantitatively evaluate the similarity between the time series of the pixels to be classified and the reference time series for the target land classes using a certain standard. Representative similarity methods include the Euclidean distance (ED) [40], [41] and dynamic time warping (DTW) methods [42], [43], [44]. Affected by factors, such as pixel deformation and sensor noise, the pixel value at a certain time in a time series of remote sensing data may be missing or abnormal. There can be large deviations when using the conventional ED to measure the similarity between pairs of unequal-length sequences. The DTW algorithm is a typical optimization method based on the concept of dynamic programming, and it is mainly used to detect the similarity between pairs of sequences. The principle of DTW is to use a time warping function that satisfies certain conditions to describe the time correspondence between the input sequence and the reference sequence. Then, the warping function corresponding to the minimum cumulative distance is solved when the two sequences match. Compared with other similarity evaluation methods, DTW overcomes the scale displacement problem to a certain extent, solves the matching problem for unequal-length time series, and can mitigate the effects of outliers to achieve an enhanced matching result for similar features. In recent years, the DTW algorithm has been combined with optical remote sensing vegetation indices and applied for the classification of remote sensing images and the classification and extraction of vegetation or land cover [45], [46], [47].

Based on the above discussion, to address the difficulties of rape planting area extraction in the South China region, we combined the compact polarimetric SAR technique to construct a dual-polarization radar index to classify the rape planting area in South China and further analyzed the influence of time series combination on the extraction accuracy of rape. To provide technical support and reference for obtaining full-coverage and high-precision monitoring results for rape planting areas. This article aims:

- 1) to construct a dual-polarized RVI based on m - χ compact polarimetric decomposition;
- 2) to extract rape planting areas based on Sentinel-1 data combined with DTW and threshold classification methods for six counties in the main rape-producing areas in the middle and lower reaches of the Yangtze River, China;
- 3) to analyze the best time series combination for rape planting area extraction using the random forest (RF) algorithm.

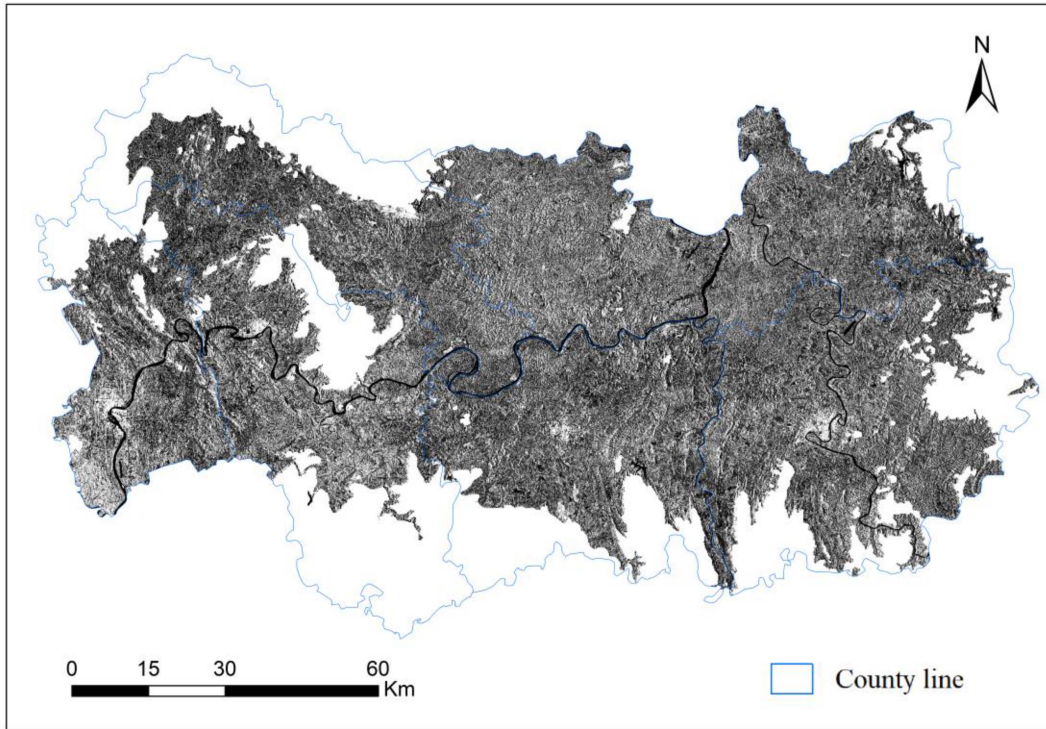


Fig. 1. Overview of the study region.

II. DATA PREPARATION AND PREPROCESSING

A. Study Region

The middle and lower reaches of the Yangtze River are the most important planting areas of rape in China. Six counties (districts) along the Xiangjiang River in Hengyang and Yongzhou cities (Qidong County, Hengnan County, Leiyang County, Changning County, Qiyang County, and Lengshuitan District) in southern Hunan Province in the middle and lower regions of the Yangtze River were selected as the study regions to verify the feasibility and applicability of regional rape planting area extraction methods based on $RVI_{m-\chi}$ and DTW threshold classification. The study region covers a total area of 12771 km². According to the *Hunan Statistical Yearbook 2020* (<http://tjj.hunan.gov.cn/hntj/index.html>), the sown area of rape in the study region is approximately 140 800 hectares, accounting for approximately one-quarter of the total sown area of rape in southern Hunan. The study region is distributed along the Xiangjiang River and is in the subtropical monsoon climate zone. The terrain of the study region is hilly, the soil type is mainly red soil, and the main crop planting system is a two-cropping system that involves winter rape and one-season rice. An overview of the study area is shown in Fig. 1. The Sentinel-1 SAR system covering the main rape-producing areas in the middle and lower reaches of the Yangtze River in China has a revisit period of 12 days. During the 160- to 200-day growth period of winter rape, at least 13 scenes of Sentinel-1 SAR images can be obtained, and $2^{13}-1$ (8191) time series combinations can be obtained. To quickly screen the optimal time series combination for extracting the rape planting area and verify the accuracy of the extraction

results, a typical test area was established in southern Qidong County, covering an area of 1024 km².






B. Remote Sensing Data

Winter rape in the study region is sown from October to mid-May of the following year. The rape seedling stage is from late November to December, and the bolting stage, flowering stage, silique stage, and maturity stage of winter rape begin in early January, mid-February, late March, and late April in the following year, respectively. The experimental remote sensing data used in this study are Sentinel-1 single look complex data, which are obtained in IW swath mode, and the polarization mode is VV+VH dual polarization. A total of 13 scenes of Sentinel-1 time series remote sensing images were used in this study, and the relative orbit number of the images was 11; additionally, the imaging dates were December 9, 2020, December 21, 2020, January 2, 2021, January 14, 2021, January 26, 2021, February 7, 2021, February 19, 2021, March 3, 2021, March 15, 2021, March 27, 2021, April 8, 2021, April 20, 2021, and May 2, 2021. Using SNAP software, the downloaded Sentinel-1 data were preprocessed, with orbit correction, radiometric calibration, band debursting, and terrain correction steps, and the spatial resolution was resampled to 20 m × 20 m. The Sentinel-1 time series images in the study region and the corresponding rape growth period are shown in Table I.

C. Ground Samples

The data acquisition date of ground sampling was March 3, 2021, which corresponds to the flowering stage when the characteristics of rape plants are more obvious than those of other

TABLE I
LIST OF SENTINEL-1 TIME SERIES IMAGES IN THE STUDY REGION

No.	Date	Absolute track number	Relative track number	Rape growth stage	Ground photo
1	20201209	035608	11	Seedling	
2	20201221	035783	11		
3	20210102	035958	11	Bolting	
4	20210114	036133	11		
5	20210126	036308	11		
6	20210207	036483	11	Flowering	
7	20210219	036658	11		
8	20210303	036833	11		
9	20210315	037008	11	Silique	
10	20210327	037183	11		
11	20210408	037358	11		
12	20210420	037533	11	Maturity	
13	20210502	037708	11		

land cover types. In the typical test area, a total of 1000 sampling points were collected, including 200 sampling points for rape, water, bare land, woodland, and buildings. The odd-numbered sampling points were used to construct the standard time series curves of the RVIs of five typical land cover types in the typical test area. The even-numbered sampling points were used to verify the accuracy of image classification and rape extraction. In addition, a total of 94 rape sampling points and 6 ground samples were collected across the entire study region to verify the accuracy of rape extraction over a large region and to further test the regional stability of $RVI_{m-\chi}$. The ground sampling points and samples were recorded, attributes were added, and transformations were projected; then, the processed samples were overlaid on the Sentinel-1 remote sensing images. The distributions of ground sampling points and samples in the study region are shown in Fig. 2.

III. METHOD

To obtain full-coverage and high-precision remote sensing monitoring results for the regional rape planting area, the dual-polarization SAR data were first decomposed by $m-\chi$ compact polarization, and the secondary scattering, volume scattering, and surface scattering components were extracted. Then, based on polarimetric decomposition, $RVI_{m-\chi}$ was constructed by using the secondary scattering, volume scattering, and surface scattering components. Finally, combined with DTW threshold

classification, the regional rape planting area was extracted from Sentinel-1 SAR data. The technical route is shown in Fig. 3, and the specific steps are as follows.

- 1) Sentinel-1 time series data were preprocessed through orbit correction, radiometric calibration, band debursting, and terrain correction steps, and the compact polarization covariance matrix (C matrix) was obtained.
- 2) $m-\chi$ compact polarimetric decomposition was performed with the C matrix from Sentinel-1 data, and the corresponding secondary scattering P_d , volume scattering P_v , and surface scattering P_s components were obtained.
- 3) $RVI_{m-\chi}$ was obtained by using P_d , P_v , and P_s . Combined with ground samples, the standard time series curves of the $RVI_{m-\chi}$ values of typical land cover types in the study region were constructed with data that fell within the 90% confidence interval at each time step.
- 4) Based on a typical sample area, the significance of the time series data was assessed using the RF algorithm, and the contribution of the data at each time point was analyzed. Optimal time series combinations were obtained.
- 5) Based on the optimal time series, referring to the standard time series curves of $RVI_{m-\chi}$ values, the DTW algorithm was used to compare the similarity between the time series curves of pixels to be classified and the standard time series curves. Based on the similarity index in DTW, the threshold value was set to conduct land cover classification.

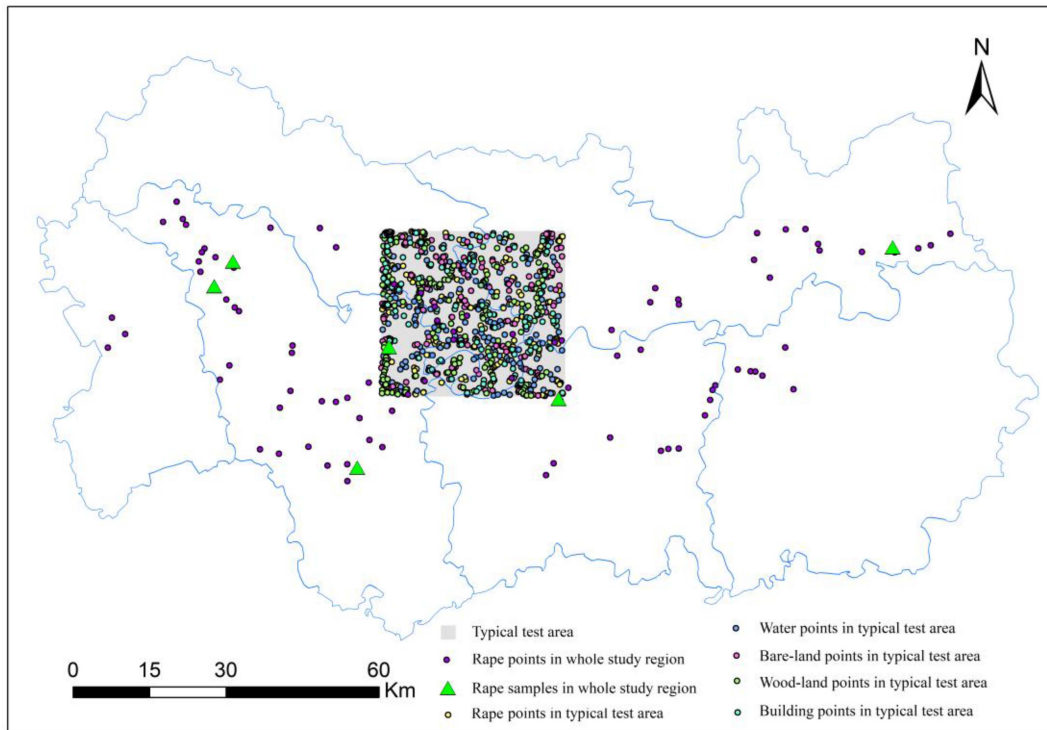


Fig. 2. Distributions of ground sampling points and samples.

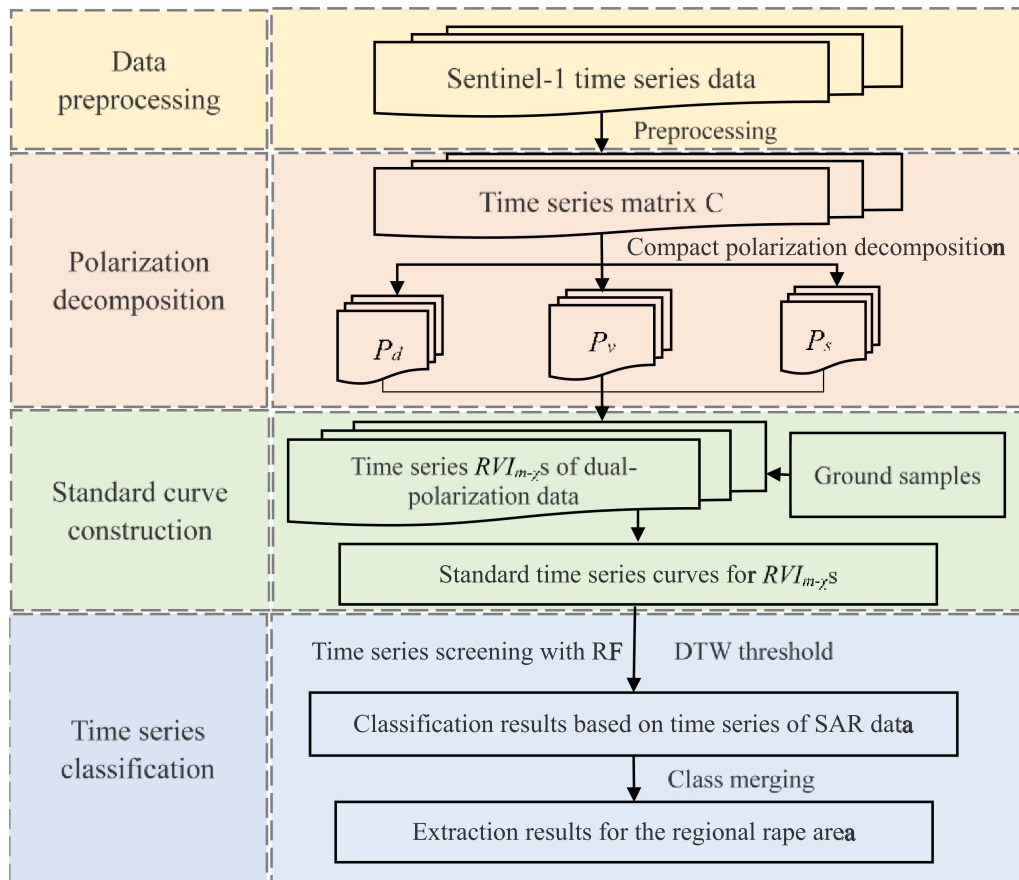


Fig. 3. Overall technical route.

Finally, the classes with the same or similar land cover were merged to obtain the results for the extraction of the rape area in the region.

A. m - χ Compact Polarimetric Decomposition and Construction of the Radar Vegetation Index

From the Stokes vector or covariance matrix, the parameters with clear physical significance can be obtained, and they include the polarization degree m , phase difference δ , and roundness χ of two orthogonal polarization components, among others [26]. Notably, m is used to characterize the random degree of scattering, δ is used to distinguish even scattering and odd scattering, and χ reflects the proportion of surface scattering to secondary scattering for fully polarized waves.

The scattering vector \vec{k}_l of VV and VH dual-polarization SAR data is

$$\vec{k}_l = \begin{bmatrix} S_{VV} \\ S_{VH} \end{bmatrix}. \quad (1)$$

Based on the scattering vector \vec{k}_l , the compact polarization covariance matrix C can be obtained as

$$C_2 = \langle \vec{k}_l \vec{k}_l^* T \rangle = \begin{bmatrix} \langle |S_{VV}|^2 \rangle & \langle S_{VV} S_{VH}^* \rangle \\ \langle S_{VH} S_{VV}^* \rangle & \langle |S_{VH}|^2 \rangle \end{bmatrix} \quad (2)$$

where $*$ indicates a complex conjugate and $\langle \cdot \rangle$ indicates the spatial statistical mean.

The Stokes vector form of VV+VH dual-polarization data is

$$g = \begin{bmatrix} g_0 \\ g_1 \\ g_2 \\ g_3 \end{bmatrix} = \begin{bmatrix} \langle |S_{VV}|^2 + |S_{VH}|^2 \rangle \\ \langle |S_{VV}|^2 - |S_{VH}|^2 \rangle \\ 2\Re \langle S_{VV} S_{VH}^* \rangle \\ -2\Im \langle S_{VV} S_{VH}^* \rangle \end{bmatrix} \quad (3)$$

where $\Re(\bullet)$ represents the real part of the complex number, $\Im(\bullet)$ represents the imaginary part of the complex number, and g_0 is the total power of the echo.

m , δ , and χ can be obtained from the Stokes vector, as shown in the following equations:

$$m = \frac{\sqrt{\sum_{i=1}^3 g_i^2}}{g_0} \quad (4)$$

$$\delta = -\arctan\left(\frac{g_3}{g_2}\right), \delta \in [-180^\circ, 180^\circ] \quad (5)$$

$$\sin 2\chi = -\frac{g_3}{mg_0}, \chi \in [-45^\circ, 45^\circ]. \quad (6)$$

The polarimetric decomposition expression based on parameters m , δ , and χ is shown in the following equations:

$$P_d = mg_0(1 + \sin 2\chi)/2 \quad (7)$$

$$P_v = (1 - m)g_0 \quad (8)$$

$$P_s = mg_0(1 - \sin 2\chi)/2 \quad (9)$$

where P_d , P_v , and P_s represent the secondary scattering component, volume scattering component, and surface scattering component, respectively, that is, the components of different scattering mechanisms for the selected scattering target.

The incident radar wave enters the vegetated area and experiences multiple scattering, and the scattering echo involves random scattering waves. The effect of vegetation on radar microwaves is mainly volume scattering. Therefore, the larger the proportion of volume scattering is to total scattering, the more likely the target is to be vegetation. To effectively distinguish rape and other typical land cover types in the study region, $RVI_{m-\chi}$ is obtained, as shown follows:

$$RVI_{m-\chi} = \frac{P_v}{P_d + P_v + P_s}. \quad (10)$$

The value range of $RVI_{m-\chi}$ is [0, 1]. When the radar signal reaches water or bare land, the volume scattering component P_v tends to zero theoretically, and the value of $RVI_{m-\chi}$ also tends to zero. When the observation area includes woodland or crops, the observed energy decreases due to single-phase scattering between the ground surface and radar microwaves that penetrate the vegetation or crop canopy and dihedral corner reflection echoes from radar microwaves at various incident angles between the ground surface and tree trunks (or plant stems); consequently, P_s and P_d decrease, and P_v increases.

B. DTW Algorithm

The central idea of the DTW algorithm is to find the optimal mapping between two given time series by dynamic adjustment and to determine the similarity of the two time series by calculating the distance between the optimal mappings (i.e., DTW distance), the smaller the distance, the higher the similarity.

The principle of the DTW algorithm is to produce two sequences $T = \{T_1, T_2, T_3, \dots, T_m\}$ and $R = \{R_1, R_2, R_3, \dots, R_n\}$ of lengths m and n , respectively. The distance matrix is defined as $D_{m \times n}$. The matrix element $d_{ij} = |\sqrt{(t_i - r_j)^2}|$ is the ED between element q_i in T and element r_j in R .

$$D_{m \times n} = \begin{bmatrix} d_{11} & d_{12} & \cdots & d_{1n} \\ d_{21} & d_{22} & \cdots & d_{2n} \\ \vdots & \vdots & \cdots & \vdots \\ d_{m1} & d_{m2} & \cdots & d_{mn} \end{bmatrix}. \quad (11)$$

In matrix $D_{m \times n}$, the set (W) of a group of adjacent matrix elements is defined as a bending path, and the starting and ending elements of the path are the two ends of the diagonal of the distance matrix and meet the relevant continuity and monotonicity constraints.

$$DTW(T, R) = \frac{1}{K} \sum_{k=1}^K w_k \quad (12)$$

where $\max(m, n) \leq K \leq m+n-1$. The DTW algorithm finds the path with the smallest cumulative distance through dynamic programming, and this path requires the shortest time to traverse.

C. Time Series Screening With the RF Algorithm

The RF method can be used to evaluate the importance of time series data, analyze the importance of the data at each point in time and optimize the time series combinations.

When evaluating the importance of time series data using an RF algorithm, it is necessary to use measurement indicators to quantify the contribution of each time series to the tree in the RF and sort the results.

In this study, the contribution of a time series is expressed by the Gini index. Assuming that there are j time series datasets $X_1, X_2, X_3, \dots, X_j$ and the RF has i trees and c categories, it is necessary to calculate the variable importance measure (VIM) of the Gini index for each feature X_j .

The Gini index of node q of the i th tree is calculated as

$$GI_q^{(i)} = \sum_{c=1}^{|C|} \sum_{c' \neq c} p_{qc}^{(i)} p_{qc'}^{(i)} = 1 - \sum_{c=1}^{|C|} \left(p_{qc}^{(i)} \right)^2 \quad (13)$$

where p_{qc} represents the proportion of category c in node q , that is, the probability that two samples are randomly selected from node q and that their category labels are inconsistent.

The importance of feature X_j in node q of the i th tree, that is, the Gini index change before and after node q branches, is

$$\text{VIM}_{jq}^{(\text{Gini})^{(i)}} = GI_q^{(i)} - GI_l^{(i)} - GI_r^{(i)} \quad (14)$$

where $GI_l^{(i)}$ and $GI_r^{(i)}$ represent the Gini indices of the two new nodes after branching.

If the node of feature X_j in decision tree i is set to Q , then the importance of X_j in the i th tree is

$$\text{VIM}_{jq}^{(\text{Gini})^{(i)}} = \sum_{q \in Q} \text{VIM}_{jq}^{(\text{Gini})^{(i)}}. \quad (15)$$

For i trees in the RF, the normalized VIM is

$$\text{VIM}_j^{(\text{Gini})} = \frac{\text{VIM}_j^{(\text{Gini})}}{\sum_{j'=1}^J \text{VIM}_{j'}^{(\text{Gini})}}. \quad (16)$$

D. Accuracy Evaluation Index

To verify the accuracy of remote sensing classification and rape planting area extraction, the overall accuracy and F1 score are selected as evaluation indicators in this study. Specifically, the overall accuracy equation is as follows:

$$A = \frac{n_0}{n} \times 100\% \quad (17)$$

where A is the overall accuracy, n_0 is the total number of rape pixels correctly extracted, and n is the total number of image pixels. The higher the overall accuracy is, the higher the extraction accuracy of the rape planting area.

The F1 score is an index used to measure the accuracy of a two-category classification model in statistics; it considers both the precision and recall of the classification model and the corresponding equation is

$$F_1 = 2 \frac{P \cdot R}{P + R} \quad (18)$$

where $P = T_p / (T_p + F_p)$ is the precision and $R = T_p / (T_p + F_n)$ is the recall. T_p , F_p , and F_n denote true positive, false positive, and false negative cases, respectively.

IV. RESULTS AND ANALYSIS

To quickly screen the optimal time series combinations extracted for the rape planting area and verify the accuracy of the extraction results, a typical test area was established in southern Qidong County, and encrypted observations of ground data were obtained during the rape flowering period. First, the characteristics of the $\text{RVI}_{m-\chi}$ curves of different land classes were analyzed based on typical test areas, and standard curves of rape were extracted. Afterward, the importance of the time-series data was analyzed based on RF, and the optimal time series was obtained. Finally, the classification results of the whole area were obtained based on the optimal time series and the DTW algorithm.

A. $\text{RVI}_{m-\chi}$ Time Series Analysis

Sentinel-1 time series data from December 2020 to May 2021 were preprocessed, and the steps included orbit correction, radiometric calibration, band debursting, and terrain correction. Then, the C matrix was obtained. $m-\chi$ compact polarimetric decomposition was performed on the C matrix of Sentinel-1 data, and the secondary scattering P_d , volume scattering P_v , and surface scattering P_s components were obtained. $\text{RVI}_{m-\chi}$ was obtained by using P_d , P_v , and P_s . Combined with ground samples, the standard time series curves of the $\text{RVI}_{m-\chi}$ values of typical land cover types in the study region were constructed based on data within the 90% confidence interval at each time step. The time series curves of five typical land cover types, including water, bare land, rape, woodland, and buildings, are shown in Fig. 4.

In previous studies, whether using Sentinel-1 data alone or using Sentinel-1 and Sentinel-2 data synergistically to extract the dryland crop planting area, the applied methods were mainly directly based on VV and VH polarized waves [2], [48], [49]. However, in southern China, the crop fields are fragmented, and the shrubs are green all year. Thus, it is very difficult to extract the planting area of tall crops such as rape based on VV or VH polarized waves. As shown in Fig. 4(a) and (b), based on the mean curves of the time series of the VV and VH bands, the temporal characteristics of rape are not prominent, and it is difficult to distinguish between rape and woodland by using these two bands directly. As shown in Fig. 4(c), for the five typical land cover types in the study region, the $\text{RVI}_{m-\chi R}$ values of water, bare land, woodland, and buildings changed slightly over time. The $\text{RVI}_{m-\chi}$ values of water and bare land were small, and the $\text{RVI}_{m-\chi}$ values of water were lower than those of bare land. Since both water and bare land are mainly characterized by surface scattering in radar images, the surface scattering component P_s was large, and the volume scattering component P_v was small. Because buildings are mainly characterized by secondary scattering and volume scattering in radar images, both the secondary scattering component P_d and volume scattering component P_v were large, thus influencing both the numerator

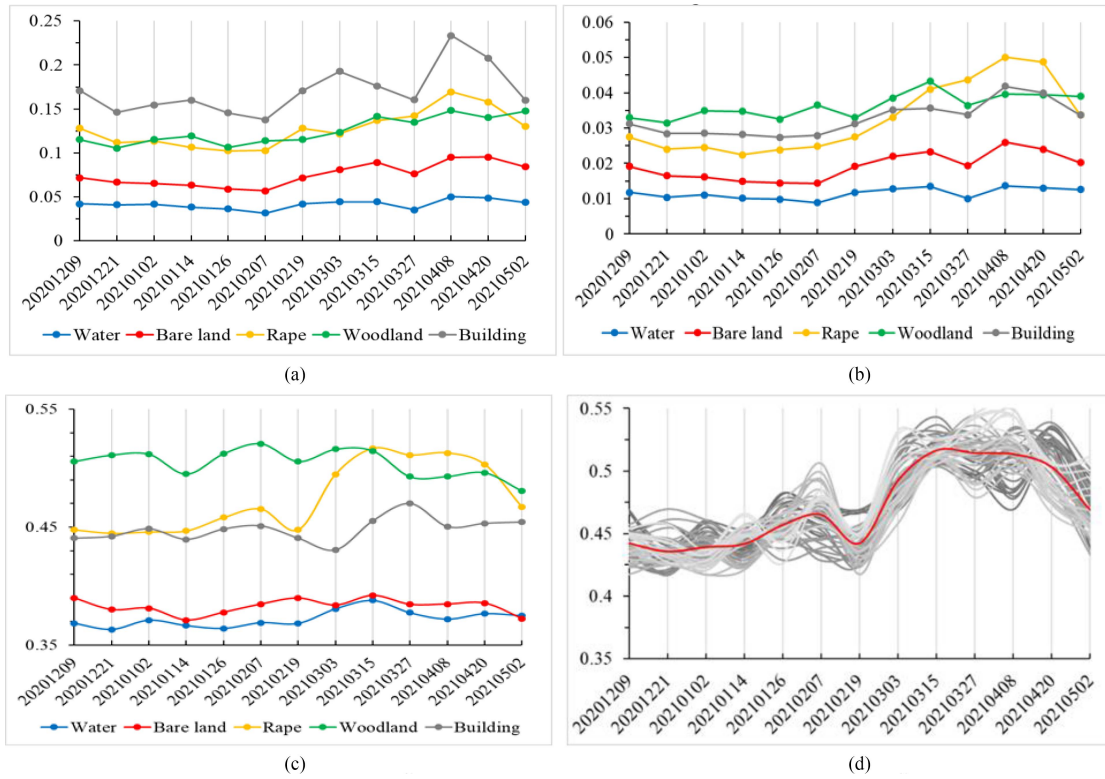


Fig. 4. Standard time series curves of the $RVI_{m-\chi}$ values of typical land cover types. (a). Standard curves of the VV band. (b). Standard curves of the VH band. (c). Standard curves of $RVI_{m-\chi}$ values. (d). Rape $RVI_{m-\chi}$ curves.

and denominator of $RVI_{m-\chi}$; consequently, the $RVI_{m-\chi}$ values of the building class were moderate. The $RVI_{m-\chi}$ values of woodland were high, mainly due to the high-volume scattering component P_v in radar images. The $RVI_{m-\chi}$ values of rape gradually increased with the growth and development of rape. Shortly after rape is sown, the plant volume is small, and the volume scattering component P_v in the radar image is small. With the flowering and silique growth of rape, the volume of rape increases, and the volume scattering component P_v also increases. Especially during the rapid growth and flowering periods (February 7, 2021 and March 15, 2021), the volume scattering component P_v of plants increases significantly, and the $RVI_{m-\chi}$ values also increase significantly. In the late stage of rape silique, the photosynthetic organs of rape gradually change from leaves into rape siliques, the leaves begin to shrink, the plant volume decreases, and the $RVI_{m-\chi}$ values also decrease. In addition, as shown in Fig. 4(d), due to the differences in rape varieties, growth environments, and field management strategies in the study region, there were also certain differences in the growth phenology of rape, especially in the flowering period and leaf shrinkage period. The above analysis suggests that $RVI_{m-\chi}$ can be used to distinguish rape and other typical land cover types from time series when applied to Sentinel-1 dual-polarization data.

B. Time Data Importance Analysis

Because of the effects of radar sensors, there was considerable coherent noise in the radar images. Increasing the number

of time-series SAR images involved in classification may not improve the accuracy of remote sensing classification and rape extraction, but it will reduce the speed and efficiency of remote sensing classification. The RF method and Gini index were used to evaluate the importance of the time series of data, and the optimal time series combination for rape extraction was selected. During the whole growth period of winter rape in the study region, 13 scenes of Sentinel-1 SAR images were obtained, and 8191 time series combinations were obtained. In this study, 500 (odd-numbered) samples obtained on the ground were used to construct the standard time series curves of the $RVI_{m-\chi}$ values of five typical land covers, and the other 500 (even-numbered) samples were used to verify the accuracy of remote sensing classification and rape extraction. The accuracy distributions for 8191 time series combinations and the contributions of 13 time series to the overall accuracy fluctuations in land cover classification and rape extraction are shown in Figs. 5 and 6, respectively.

Based on the accuracy distributions of image classification and rape extraction in Fig. 5, the overall accuracy of image classification varies from 46.4% to 63.0%, mainly ranging from 51% to 60%, and the overall accuracy of rape extraction varies from 22% to 75%, mainly ranging from 61% to 70%. The overall accuracy of remote sensing image classification was less affected by the time series combination selected, and the lowest accuracy was greater than 50%. The overall accuracy of rape extraction was greatly affected by the time series combination selected, and it was necessary to further clarify the optimal time series combination to improve the rape extraction

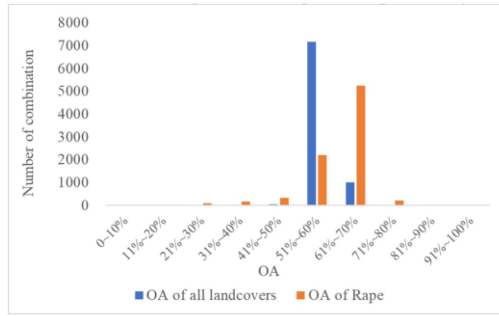


Fig. 5. Accuracy distributions for image classification and rape extraction.

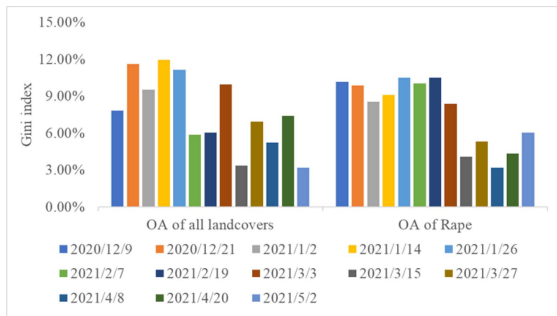
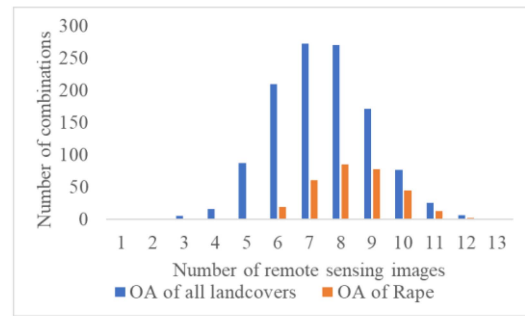


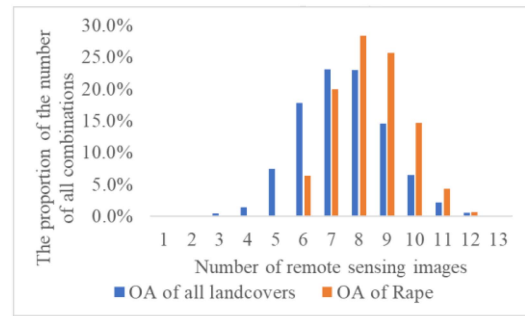
Fig. 6. Contributions of time series to overall accuracy fluctuations.

accuracy and operation efficiency of the applied classification algorithm.

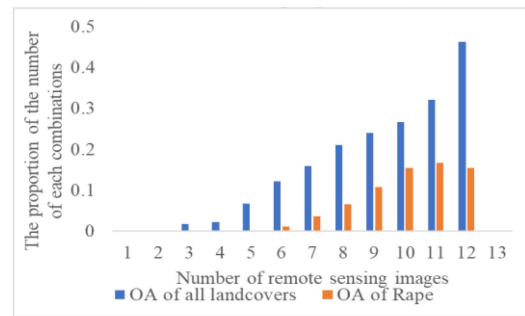
The contributions of the 13 time series to the overall accuracy fluctuations in image classification and rape extraction are shown in Fig. 6. The variations in images at different times have a considerable influence on the accuracy of remote sensing classification and rape extraction. From Fig. 6, the five time series that contributed the most to the fluctuations in the accuracy of image classification were those on January 14, 2021, December 21, 2020, January 26, 2021, March 3, 2021, and January 2, 2021; additionally, the five time series that contributed the most to the fluctuations in the accuracy of rape extraction were those on February 19, 2021, January 26, 2021, December 9, 2020, February 7, 2021, and December 21, 2020. Most of the data that highly contribute to fluctuations in the overall accuracy of image classification and rape extraction were from the rape seedling stage. On the one hand, the plant characteristics of rape in the seedling stage are not significantly different from those of other land cover types, and rape is especially easily confused with bare land. On the other hand, the rape seedling and bolting stages occur in winter and early spring, and the differences in characteristics among typical land cover types are quite large in the study region, especially those for water and bare land. The above two factors have a combined effect on the classification results, highlighting the influence of SAR data from the rape seedling and bolting stages on the accuracy of remote sensing and the accuracy of rapeseed extraction. From a comprehensive perspective considering multiple factors, the acquisition of high-quality SAR remote sensing images in the rape seedling and bolting stages has a positive effect on both rape extraction and image classification.



(a)



(b)



(c)

Fig. 7. Time series data distributions for high-accuracy combinations. (a) Absolute quantity. (b) Absolute proportion. (c) Relative quantity.

C. Time Series Screening

First, an overall accuracy of remote sensing classification greater than 60% and an overall accuracy of rape extraction greater than 70% were selected as indicators, and further analysis was performed on each time series to obtain the optimal time series combinations. There were 1178 time series combinations with an overall accuracy of remote sensing classification greater than 60% and 300 time series combinations with an overall accuracy of rape extraction greater than 70%. The time series data distributions for the high-accuracy combinations are shown in Fig. 7.

Based on the distributions of high-accuracy time series combinations in Fig. 7(a) and the proportional distributions of high-accuracy time series combinations in Fig. 7(b), the time series combinations with an overall accuracy of image classification greater than 60% mainly included data from seven or eight scenes. Moreover, the time series combinations with an overall accuracy of rape extraction greater than 70% mainly included data from eight or nine scenes. As shown in Fig. 7(c), the proportion of high-accuracy time series combinations among all

TABLE II
LIST OF HIGH-ACCURACY TIME SERIES COMBINATIONS

	No.	Date													
		12 09	12 21	01 02	01 14	01 26	02 07	02 19	03 03	03 15	03 27	04 08	04 20	05 02	
High OA for rape	1	1	0	1	0	0	1	0	1	1	1	1	0	1	
	2	0	0	1	1	1	0	1	0	1	1	1	1	1	
	3	0	0	1	1	0	1	1	1	1	0	1	0	1	
	4	0	0	0	1	0	0	1	1	1	0	1	0	1	
	5	0	0	0	1	0	0	1	1	1	1	1	1	1	
	6	1	0	1	1	0	1	1	1	1	0	1	0	1	
	7	0	0	1	1	1	0	1	1	1	1	1	1	1	
	8	1	0	1	0	0	1	0	1	1	0	1	0	1	
	9	1	0	0	1	0	1	0	1	1	0	1	0	1	
High OA for all landcover types	10	0	1	1	0	0	1	0	1	1	1	1	0	0	
	11	0	1	1	0	0	0	0	1	1	1	0	1	0	
	12	0	1	0	0	0	1	1	1	1	1	0	1	0	
	13	0	0	1	0	1	0	0	1	1	1	0	1	0	
	14	1	1	0	0	0	1	0	1	1	1	1	0	0	
	15	0	1	0	0	0	1	1	1	1	1	1	0	0	
	16	0	0	1	0	0	1	1	1	1	1	1	0	0	
	17	0	0	1	0	0	1	1	1	1	1	1	0	0	
	18	0	1	1	0	0	1	0	0	1	1	0	1	0	

TIP: 1 indicates that the time data were used, and 0 indicates that the time data were not used.

the obtained time series combinations showed that the overall accuracy of image classification increased with the amount of data contained in the time series combinations, and the overall accuracy of rape extraction first increased and then decreased slightly as the amount of data contained in the time series combinations increased. That is, the larger the amount of data contained in the time series combinations was, the higher the overall accuracy of image classification and rape extraction. If limited data were considered in a time series combination, the features between rape and other land cover types could not be effectively distinguished; conversely, considering too much data could introduce redundant information and lead to increased classification errors.

Based on the image classification and rape extraction results, nine time series combinations with high classification or extraction accuracy were selected for analysis. The classification results are shown in Table II and Fig. 8, and the classification accuracy is shown in Table III.

As shown in Fig. 8, for combinations that yielded high rape extraction accuracy or high image classification accuracy, the classification results for the rape planting area in the typical test area were satisfactory, and the accuracy of rape extraction was higher than that of image classification. The overall classification accuracy was affected by the confusion of water and bare land. Notably, both water and bare land are characterized by surface scattering in radar images, and the $RVI_{m-\chi}$ values were low for both. Moreover, the study region was in a hilly area, and the complex terrain interfered with the radar microwave signals. In addition, the time series classification results involve the synthesis of multiple time series features for classification. Bare

land in the seedling stage of rape might store water and be used to plant early rice when the rape is mature.

Tables II and III indicate that all the time series combinations that yielded high rape extraction accuracy included the remote sensing data obtained from March 15, 2021, April 8, 2021, and May 2, 2021; these dates corresponded to the blooming, silique, and maturity stages of rape, respectively. At these times, rape plants were characterized by unique flowers or siliques, which had characteristics that obviously differed from those of other vegetation types and were highly distinguishable. Thus, the data collected at the above times and used in image classification increased the accuracy of rape extraction. Most of the time series combinations that yielded high rape extraction accuracy included remote sensing data obtained on January 2, 2021, January 14, 2021, February 19, 2021, and March 3, 2021; these dates corresponded to the rape bolting and flowering stages. At these times, the characteristics of rape plants and typical land cover types such as woodland and buildings were highly different; therefore, including the corresponding data in remote sensing classification improved the accuracy of rape extraction. Most of the time series combinations that yielded high image classification accuracy included remote sensing data obtained on December 21, 2020, January 2, 2021, February 7, 2021, March 3, 2021, March 15, 2021, and March 27, 2021; these dates can be divided into two time periods corresponding to winter and early spring in the study region. In winter and early spring, the differences in the characteristics of typical land cover types in the study region are quite large, especially for water and bare land; therefore, the data collected at the above times and used in image classification increased the classification accuracy.

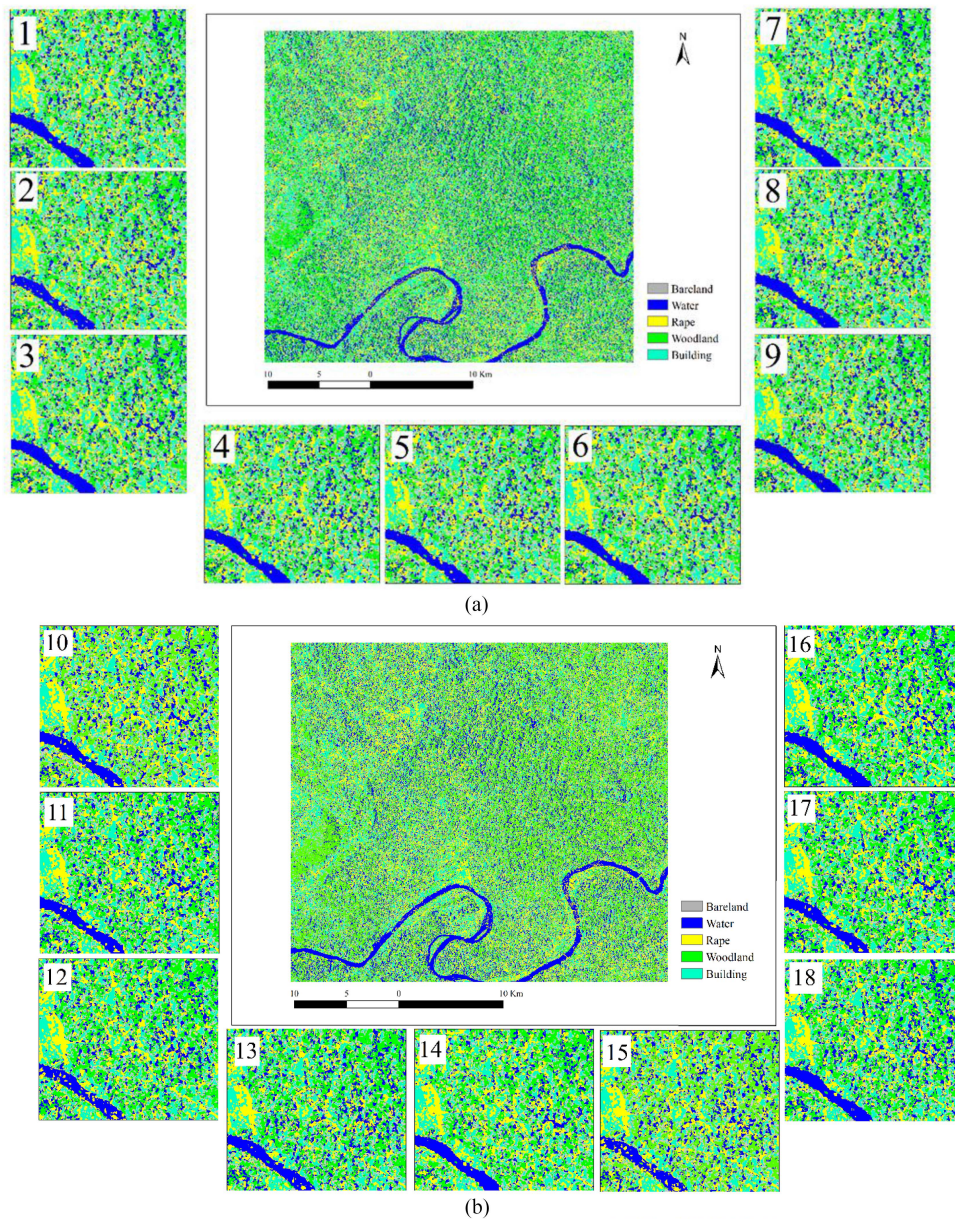


Fig. 8. High-accuracy classification results in typical test areas. (a) Classification results for nine time series combinations that yielded high-accuracy rape extraction. (b) Classification results for nine time series combinations that yielded high-accuracy image classification.

D. Classification Results for the Entire Study Area

To analyze the stability of the $RVI_{m-\chi}$ values and the regional expansion capability of the proposed classification method, the $RVI_{m-\chi}$ time series curves for typical land cover types constructed based on the typical test area were extended to image classification and rape planting area extraction in the entire study region. In the selection of time series combinations, the accuracy (the overall accuracy of image classification was greater than 60%, and the overall accuracy of rape extraction was greater than 70%) and efficiency (the amount of data contained in the time series combinations was minimized, and early data were prioritized) of image classification and rape extraction were considered. A combination of six time series obtained on January 2, 2021, February 7, 2021, February 19, 2021, March 3, 2021,

March 15, 2021, and March 27, 2021, were used to conduct remote sensing classification and rape extraction in the entire study region, and the classification results are shown in Fig. 9.

The accuracy of the rape extraction results in the study area was verified based on 94 rape sampling points and 6 ground samples collected on March 3. Among the 94 rape sampling points established in the field, rape was accurately classified at 74 points, with an overall accuracy of 78.72%. Six ground samples were used to verify the accuracy of rape extraction. The ground samples and the rape extraction accuracy results are shown in Fig. 10 and Table IV.

Based on the ground samples in Fig. 10, most of the rape plots were accurately classified as rape, and some rape and other land cover types were misclassified. The rape extraction results in Table IV indicate that the F-1 coefficient ranged from 58.68% to

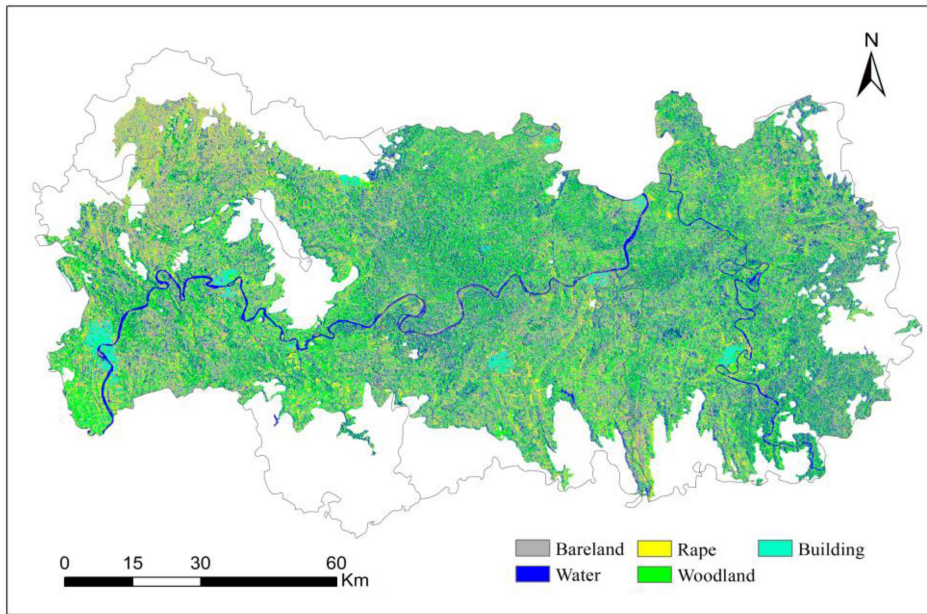


Fig. 9. Remote sensing classification results for the study region.

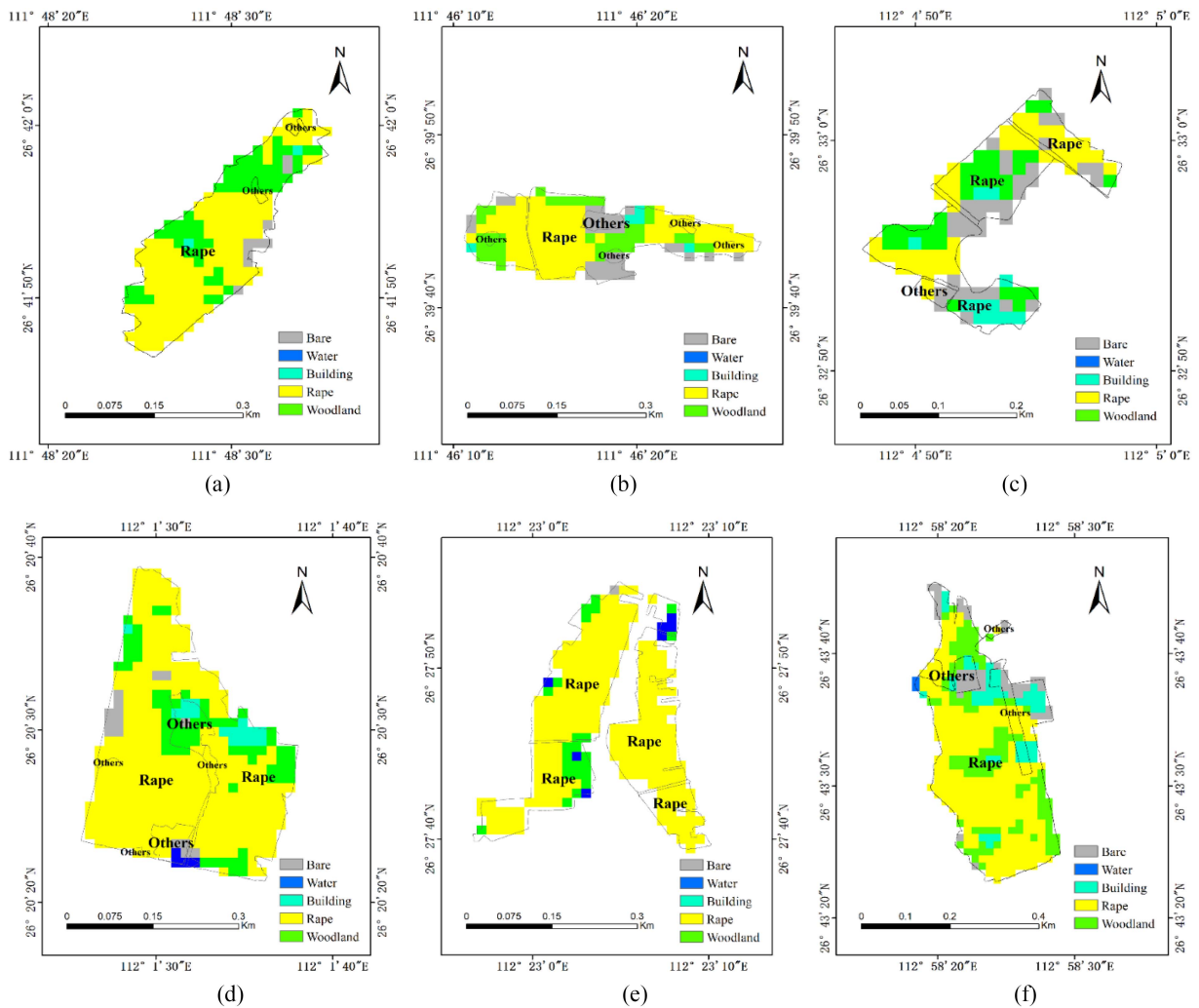


Fig. 10. Ground samples. (a) Sample 1. (b) Sample 2. (c) Sample 3. (d) Sample 4. (e) Sample 5. (f) Sample 6.

TABLE III
HIGH-ACCURACY CLASSIFICATION ACCURACIES IN TYPICAL TEST AREAS

	No.	OA for all landcover types	OA for rape	TP	TN	FP	FN	F-1 score for rape
High OA for rape	1	61.80%	75.00%	75	351	25	49	66.96%
	2	60.00%	74.00%	74	353	26	47	66.97%
	3	61.00%	74.00%	74	351	27	49	66.07%
	4	60.60%	74.00%	74	355	26	45	67.58%
	5	60.20%	74.00%	74	354	26	46	67.27%
	6	60.60%	73.00%	73	356	27	44	67.28%
	7	60.60%	73.00%	73	352	27	48	66.06%
	8	62.00%	73.00%	73	355	27	45	66.97%
	9	61.20%	73.00%	73	353	27	46	66.67%
High OA for all landcover types	10	63.00%	66.00%	66	355	34	45	62.56%
	11	62.60%	67.00%	67	353	33	47	62.62%
	12	62.40%	68.00%	68	353	32	47	63.26%
	13	62.40%	64.00%	64	351	36	49	60.09%
	14	62.40%	69.00%	69	357	31	43	65.09%
	15	62.20%	67.00%	67	355	33	45	63.21%
	16	62.20%	70.00%	70	352	30	48	64.22%
	17	62.20%	68.00%	68	352	32	48	62.96%
	18	62.00%	67.00%	67	353	33	47	62.62%

TABLE IV
ACCURACY OF RAPE PLANTING AREA EXTRACTION IN THE STUDY REGION

	Sample 1	Sample 2	Sample 3	Sample 4	Sample 5	Sample 6	Total
TP	141	100	49	328	235	253	1106
TN	2	1	2	21	0	24	50
FP	66	67	68	75	47	174	497
FN	6	2	1	3	0	10	22
Precision	68.12%	59.88%	41.88%	81.39%	83.33%	59.25%	69.00%
Recall	95.92%	98.04%	98.00%	99.09%	100.00%	96.20%	98.05%
F-1 score	79.66%	74.35%	58.68%	89.37%	90.91%	73.33%	81.00%

91.26%. Sample 3 yielded the lowest overall accuracy, and the F-1 coefficient was the smallest among those of the six ground samples. Because the spatial resolution of the Sentinel-1 image was only 20 m, the feature recognition ability of small plots was relatively poor. Overall, the F-1 coefficient of the 6 ground samples was 81.00%. The rape planting area extraction method based on $RVI_{m-\chi}$ and DTW threshold classification yielded high accuracy in regional rape planting area extraction; this result further highlighted the stability of $RVI_{m-\chi}$ and the feasibility of applying DTW time series classification in the time series extraction of the rape planting area.

V. DISCUSSION

A. $RVI_{m-\chi}$ Can Reflect the Temporal Variations in Rape Plants

In previous studies, whether using Sentinel-1 data alone or Sentinel-1 and Sentinel-2 data synergistically to extract dryland crop planting areas, the applied methods were mainly directly based on VV and VH polarized waves [2], [48], [49]. However, in

southern China, the crop fields are fragmented, and the shrubs are green year round. Thus, it is very difficult to extract the planting area of tall crops such as rape based on VV or VH polarized waves. In this study, based on $m-\chi$ compact polarimetric decomposition, for Sentinel-1 dual-polarization SAR data, a new dual-polarization RVI was constructed based on $m-\chi$ decomposition, and it was used to distinguish rape and other typical land cover types in time series. From the experimental results and analysis, the $RVI_{m-\chi}$ values of water, bare land, woodland, and buildings changed slightly, while the $RVI_{m-\chi}$ values of rape changed greatly over time. The $RVI_{m-\chi}$ values of rape gradually increased with the growth and development of rape. When rape was just sown, the plant volume was small, and the volume scattering component P_v in the radar images was small. With the flowering and silique growth of rape, the volume of rape increased, and the volume scattering component P_v also increased. Notably, during the rapid growth and flowering periods of rape (February 7, 2021 and March 15, 2021), the volume scattering component P_v of plants increased significantly, and the $RVI_{m-\chi}$ values also

increased significantly. In the late stage of rape silique, the photosynthetic organs of rape gradually changed from leaves to rape siliques, the leaves began to shrink, the plant volume decreased, and the $RVI_{m-\chi}$ values also decreased. Overall, the temporal variations in rape $RVI_{m-\chi}$ values reflect the temporal variations in rape plant characteristics.

B. Data From Different Times Have a Large Impact on the RVI and DTW Threshold Classification Methods

Because of the effects of radar sensors, there was considerable coherent noise in the radar images. Increasing the number of time-series SAR images involved in classification may not improve the accuracy of remote sensing classification and rape extraction, but it will reduce the speed and efficiency of remote sensing classification. In this study, the RF method and Gini index were used to evaluate the importance of the time series of data and the optimal time series combination for rape extraction was selected. Most of the data that highly contribute to fluctuations in the overall accuracy of image classification and rape extraction were from the rape seedling stage. On the one hand, the plant characteristics of rape in the seedling stage are not significantly different from those of other land cover types, and rape is especially easily confused with bare land. On the other hand, the rape seedling and bolting stages occur in winter and early spring, and the differences in the characteristics of typical land cover types are notable in the study region, especially those for water and bare land. The above two factors have a combined effect on the classification results, highlighting the influence of SAR data from the rape seedling and bolting stages on the classification accuracy of remote sensing and the accuracy of rapeseed extraction. From a comprehensive perspective considering multiple factors, the acquisition of high-quality SAR remote sensing images in the rape seedling and bolting stages has a positive effect on both rape extraction and image classification. Moreover, the greater the amount of data contained in time series combinations is, the higher the overall accuracy of image classification and rape extraction. If limited data are considered in a time series combination, the features of rape and other land cover types cannot be effectively distinguished; conversely, considering too much data can introduce redundant information and lead to increased classification errors.

C. Shortcomings of This Research and Future Plans

For the main area of rape production in southern Hunan Province, the extraction of the regional rape planting area was performed based on the $RVI_{m-\chi}$ method and DTW threshold classification. The proposed methods are generally applicable to other main rapeseed-producing areas in China where remote sensing images are affected by clouds, rain, and fog and contain gaps in optical data. However, the method of regional rape area extraction implemented in this study has certain shortcomings. Rape plants are tall and densely distributed in the middle and lower reaches of the Yangtze River in China. When $RVI_{m-\chi}$ is used in analyses of other crops, to effectively adapt to the characteristics of crops in regional crop mapping, it may be necessary to introduce a parameter [33]. Therefore, in future research, more crop varieties and sowing methods need to be

considered, and verification of the accuracy and applicability of the crop area extraction method based on $RVI_{m-\chi}$ should be performed over large study regions. In addition, it is also possible to consider combining the $RVI_{m-\chi}$ index with other classification algorithms, such as machine learning algorithms, in the future. The improvement of the extraction method may effectively improve the classification accuracy.

VI. CONCLUSION

To obtain full-coverage and high-precision remote sensing monitoring results for the rape planting area, the remote sensing classification of rape planting areas was performed based on a dual-polarization RVI, and the influence of time series combination on the extraction accuracy of rape in South China was further analyzed. First, based on $m-\chi$ compact polarimetric decomposition, a dual-polarization RVI was constructed. Then, for six counties in Hengyang and Yongzhou, the main rape-producing areas in the middle and lower reaches of the Yangtze River in China, based on the DTW and threshold classification methods, Sentinel-1 remote sensing extraction of the regional rape planting area was performed. Finally, an RF algorithm was used to analyze and screen the optimal time series combination of the extracted regional rape planting areas. The research results showed that in a typical test area, based on the accuracy of remote sensing classification and rape extraction obtained for different time series combinations, $RVI_{m-\chi}$ could be effectively used to distinguish rape from other typical land cover types when applied to Sentinel-1 dual-polarization data. Additionally, high-quality SAR remote sensing images from the bolting stage of rape enhanced the accuracy of both rape extraction and image classification. It is easier to obtain high-precision rape area extraction results by using time series combinations with 8 scenes with obvious features of rape plants, such as those from the flowering stage, silique stage, and maturity stage. With Sentinel-1 time series data from January 2, 2021, February 7, 2021, February 19, 2021, March 3, 2021, March 15, 2021, and March 27, 2021, and based on the $RVI_{m-\chi}$ standard time series curves of typical land cover types constructed in the typical test region, the proposed approach was extended to remote sensing classification and rape planting area extraction in the whole study area. Among the 94 rape sampling points selected in the field, rape was correctly classified at 74 sampling points, and the overall accuracy was 78.72%. Moreover, six ground samples were used to verify the accuracy of the rape planting area extraction results, and the rape F-1 score was 81.00%. The above results indicated that the rape planting area extraction method based on $RVI_{m-\chi}$ and DTW threshold classification yielded high accuracy in regional rape planting area extraction and verified the regional expansion capability of the $RVI_{m-\chi}$ approach. This study can provide technical support for the realization of full-coverage and high-precision remote sensing monitoring in the main rape-producing areas in China.

REFERENCES

- [1] M. van der Velde, F. Bouraoui, and A. Aloe, "Pan-European regional-scale modelling of water and N efficiencies of rapeseed cultivation for biodiesel production," *Glob. Change Biol.*, vol. 15, no. 1, pp. 24–37, Jan. 2009, doi: 10.1111/j.1365-2486.2008.01706.x.

- [2] R. d'Andrimont, M. Taymans, G. Lemoine, A. Ceglar, M. Yordanov, and M. van der Velde, "Detecting flowering phenology in oil seed rape parcels with Sentinel-1 and -2 time series," *Remote Sens. Environ.*, vol. 239, Mar. 2020, Art. no. 111660, doi: [10.1016/j.rse.2020.111660](https://doi.org/10.1016/j.rse.2020.111660).
- [3] Z. K. Pan, J. F. Huang, and F. M. Wang, "Multi range spectral feature fitting for hyperspectral imagery in extracting oilseed rape planting area," *Int. J. Appl. Earth Observ. Geoinf.*, vol. 25, pp. 21–29, Dec. 2013, doi: [10.1016/j.jag.2013.03.002](https://doi.org/10.1016/j.jag.2013.03.002).
- [4] S. M. Chen et al., "Two-stepwise hierarchical adaptive threshold method for automatic rapeseed mapping over Jiangsu using harmonized Landsat/Sentinel-2," *Remote Sens.*, vol. 14, no. 11, Jun. 2022, Art. no. 2715, doi: [10.3390/rs14112715](https://doi.org/10.3390/rs14112715).
- [5] J. Betbeder, R. Fieuzal, Y. Philipplets, L. Ferro-Famil, and F. Baup, "Contribution of multitemporal polarimetric synthetic aperture radar data for monitoring winter wheat and rapeseed crops," *J. Appl. Remote Sens.*, vol. 10, May 2016, Art. no. 026020, doi: [10.1117/1.Jrs.10.026020](https://doi.org/10.1117/1.Jrs.10.026020).
- [6] C. A. Liu, Z. X. Chen, Y. Shao, J. S. Chen, T. Hasi, and H. Z. Pan, "Research advances of SAR remote sensing for agriculture applications: A review," *J. Integr. Agriculture*, vol. 18, no. 3, pp. 506–525, Mar. 2019, doi: [10.1016/s2095-3119\(18\)62016-7](https://doi.org/10.1016/s2095-3119(18)62016-7).
- [7] H. McNairn and J. L. Shang, "A review of multitemporal synthetic aperture radar (SAR) for crop monitoring," *Multitemporal Remote Sens., Methods Appl.*, vol. 20, pp. 317–340, 2016, doi: [10.1007/978-3-319-47037-5_15](https://doi.org/10.1007/978-3-319-47037-5_15).
- [8] T. Sivasankar, D. Kumar, H. Srivastava, and P. Patel, "Advances in radar remote sensing of agricultural crops: A review," *Int. J. Adv. Sci., Eng. Inf. Technol.*, vol. 8, Aug. 2018, pp. 1126–1137, doi: [10.18517/ija-seit.8.4.5797](https://doi.org/10.18517/ija-seit.8.4.5797).
- [9] G. Satalino, A. Balenzano, F. Mattia, and M. W. J. Davidson, "C-Band SAR data for mapping crops dominated by surface or volume scattering," *IEEE Geosci. Remote Sens. Lett.*, vol. 11, no. 2, pp. 384–388, Feb. 2014, doi: [10.1109/lgrs.2013.2263034](https://doi.org/10.1109/lgrs.2013.2263034).
- [10] S. Kraatz et al., "Comparison between dense L-band and C-band synthetic aperture radar (SAR) time series for crop area mapping over a NISAR calibration-validation site," *Agronomy*, vol. 11, no. 2, Feb. 2021, Art. no. 273, doi: [10.3390/agronomy11020273](https://doi.org/10.3390/agronomy11020273).
- [11] H. K. Hoang, M. Bernier, S. Duchesne, and Y. M. Tran, "Rice mapping using RADARSAT-2 dual- and quad-pol data in a complex land-use watershed: Cau River basin (Vietnam)," *IEEE J. Sel. Topics Appl. Earth Observ. Remote Sens.*, vol. 9, no. 7, pp. 3082–3096, Jul. 2016, doi: [10.1109/jstars.2016.2586102](https://doi.org/10.1109/jstars.2016.2586102).
- [12] K. Lasko, K. P. Vadrevu, V. T. Tran, and C. Justice, "Mapping double and single crop paddy rice with Sentinel-1A at varying spatial scales and polarizations in Hanoi, Vietnam," *IEEE J. Sel. Topics Appl. Earth Observ. Remote Sens.*, vol. 11, no. 2, pp. 498–512, Feb. 2018, doi: [10.1109/jstars.2017.2784784](https://doi.org/10.1109/jstars.2017.2784784).
- [13] G. Fontanelli et al., "Early-season crop mapping on an agricultural area in Italy using X-band dual-polarization SAR satellite data and convolutional neural networks," *IEEE J. Sel. Topics Appl. Earth Observ. Remote Sens.*, vol. 15, pp. 6789–6803, 2022, doi: [10.1109/jstars.2022.3198475](https://doi.org/10.1109/jstars.2022.3198475).
- [14] W. F. Zhang et al., "Compact polarimetric response of rape (*Brassica napus* L.) at C-band: Analysis and growth parameters inversion," *Remote Sens.*, vol. 9, no. 6, Jun. 2017, Art. no. 591, doi: [10.3390/rs9060591](https://doi.org/10.3390/rs9060591).
- [15] R. Torres et al., "GMES Sentinel-1 mission," *Remote Sens. Environ., Interdiscipl. J.*, vol. 120, pp. 9–24, May 2012, doi: [10.1016/j.rse.2011.05.028](https://doi.org/10.1016/j.rse.2011.05.028).
- [16] S. R. Wu, J. Q. Ren, Z. X. Chen, P. Yang, and H. Li, "Soil moisture estimation based on the microwave scattering mechanism during different crop phenological periods in a winter wheat-producing region," *J. Hydrol.*, vol. 590, Nov. 2020, Art. no. 125521, doi: [10.1016/j.jhydrol.2020.125521](https://doi.org/10.1016/j.jhydrol.2020.125521).
- [17] S. R. Wu, P. Yang, J. Q. Ren, Z. X. Chen, C. G. Liu, and H. Li, "Winter wheat LAI inversion considering morphological characteristics at different growth stages coupled with microwave scattering model and canopy simulation model," *Remote Sens. Environ.*, vol. 240, Apr. 2020, Art. no. 111681, doi: [10.1016/j.rse.2020.111681](https://doi.org/10.1016/j.rse.2020.111681).
- [18] N. Bhogapurapu et al., "Dual-polarimetric descriptors from Sentinel-1 GRD SAR data for crop growth assessment," *ISPRS J. Photogramm. Remote Sens.*, vol. 178, pp. 20–35, Aug. 2021, doi: [10.1016/j.isprsjprs.2021.05.013](https://doi.org/10.1016/j.isprsjprs.2021.05.013).
- [19] K. Li, B. Brisco, S. Yun, and R. Touzi, "Polarimetric decomposition with RADARSAT-2 for rice mapping and monitoring," *Can. J. Remote Sens.*, vol. 38, no. 2, pp. 169–179, Apr. 2012, doi: [10.5589/m12-024](https://doi.org/10.5589/m12-024).
- [20] P. J. Du, A. Samat, B. Waske, S. C. Liu, and Z. H. Li, "Random forest and rotation forest for fully polarized SAR image classification using polarimetric and spatial features," *ISPRS J. Photogramm. Remote Sens.*, vol. 105, pp. 38–53, Jul. 2015, doi: [10.1016/j.isprsjprs.2015.03.002](https://doi.org/10.1016/j.isprsjprs.2015.03.002).
- [21] J. Guo, P.-L. Wei, J. Liu, B. Jin, B.-F. Su, and Z.-S. Zhou, "Crop classification based on differential characteristics of H/alpha scattering parameters for multitemporal quad- and dual-polarization SAR images," *IEEE Trans. Geosci. Remote Sens.*, vol. 56, no. 10, pp. 6111–6123, Oct. 2018, doi: [10.1109/tgrs.2018.2832054](https://doi.org/10.1109/tgrs.2018.2832054).
- [22] C. Yang, B. Hou, B. Ren, Y. Hu, and L. C. Jiao, "CNN-based polarimetric decomposition feature selection for PolSAR image classification," *IEEE Trans. Geosci. Remote Sens.*, vol. 57, no. 11, pp. 8796–8812, Nov. 2019, doi: [10.1109/tgrs.2019.2922978](https://doi.org/10.1109/tgrs.2019.2922978).
- [23] G. G. Ponnurangam and Y. S. Rao, "The application of compact polarimetric decomposition algorithms to L-band PolSAR data in agricultural areas," *Int. J. Remote Sens.*, vol. 39, no. 22, pp. 8337–8360, Feb. 2018, doi: [10.1080/01431161.2018.1488281](https://doi.org/10.1080/01431161.2018.1488281).
- [24] Q. X. Xie, Q. Y. Meng, L. L. Zhang, C. M. Wang, Q. Wang, and S. H. Zhao, "Combining of the H/A/alpha and Freeman–Durden polarization decomposition methods for soil moisture retrieval from full-polarization Radarsat-2 data," *Adv. Meteorol.*, vol. 2018, 2018, Art. no. 9436438, doi: [10.1155/2018/9436438](https://doi.org/10.1155/2018/9436438).
- [25] W. T. Zhang, M. Wang, J. Guo, and S. T. Lou, "Crop classification using MSCDN classifier and sparse auto-encoders with non-negativity constraints for multi-temporal, quad-pol SAR data," *Remote Sens.*, vol. 13, no. 14, Jul. 2021, doi: [10.3390/rs13142749](https://doi.org/10.3390/rs13142749).
- [26] R. K. Raney, "Hybrid-polarity SAR architecture," in *Proc. IEEE Int. Symp. Geosci. Remote Sens.*, 2006, pp. 3846–3848.
- [27] S. R. Cloude, D. G. Goodenough, and H. Chen, "Compact decomposition theory," *IEEE Geosci. Remote Sens. Lett.*, vol. 9, no. 1, pp. 28–32, Jan. 2012, doi: [10.1109/lgrs.2011.2158983](https://doi.org/10.1109/lgrs.2011.2158983).
- [28] R. K. Raney, J. T. S. Cahill, G. W. Patterson, and D. B. J. Bussey, "The m-chi decomposition of hybrid dual-polarimetric radar data with application to lunar craters," *J. Geophys. Res., Planets*, vol. 117, May 2012, Art. no. E00H21, doi: [10.1029/2011je003986](https://doi.org/10.1029/2011je003986).
- [29] S. Homayouni, H. McNairn, M. Hosseini, X. Jiao, and J. Powers, "Quad and compact multitemporal C-band PolSAR observations for crop characterization and monitoring," *Int. J. Appl. Earth Observ. Geoinf.*, vol. 74, pp. 78–87, Feb. 2019, doi: [10.1016/j.jag.2018.09.009](https://doi.org/10.1016/j.jag.2018.09.009).
- [30] M. Mahdianpari et al., "Mid-season crop classification using dual-, compact-, and full-polarization in preparation for the RADARSAT Constellation Mission (RCM)," *Remote Sens.*, vol. 11, no. 13, Jul. 2019, Art. no. 1582, doi: [10.3390/rs11131582](https://doi.org/10.3390/rs11131582).
- [31] V. Kumar, D. Mandal, A. Bhattacharya, and Y. S. Rao, "Crop characterization using an improved scattering power decomposition technique for compact polarimetric SAR data," *Int. J. Appl. Earth Observ. Geoinf.*, vol. 88, Jun. 2020, Art. no. 102052, doi: [10.1016/j.jag.2020.102052](https://doi.org/10.1016/j.jag.2020.102052).
- [32] D. Mandal et al., "A radar vegetation index for crop monitoring using compact polarimetric SAR data," *IEEE Trans. Geosci. Remote Sens.*, vol. 58, no. 9, pp. 6321–6335, Sep. 2020, doi: [10.1109/TGRS.2020.2976661](https://doi.org/10.1109/TGRS.2020.2976661).
- [33] D. Mandal et al., "Dual polarimetric radar vegetation index for crop growth monitoring using Sentinel-1 SAR data," *Remote Sens. Environ.*, vol. 247, Sep. 2020, Art. no. 111954, doi: [10.1016/j.rse.2020.111954](https://doi.org/10.1016/j.rse.2020.111954).
- [34] Y. Kim and J. van Zyl, "Comparison of forest parameter estimation techniques using SAR data," in *Proc. Scanning Present Resolving Future, IEEE Int. Geosci. Remote Sens. Symp.*, 2001, vol. 3, pp. 1395–1397.
- [35] Y. Kim and J. J. van Zyl, "A time-series approach to estimate soil moisture using polarimetric radar data," *IEEE Trans. Geosci. Remote Sens.*, vol. 47, no. 8, pp. 2519–2527, Aug. 2009, doi: [10.1109/tgrs.2009.2014944](https://doi.org/10.1109/tgrs.2009.2014944).
- [36] X. Mei, W. Nie, J. Y. Liu, and K. Huang, "PolSAR image crop classification based on deep residual learning network," in *Proc. 7th Int. Conf. Agro-Geoinform.*, 2018, pp. 1–6.
- [37] M. Li and W. Bijker, "Vegetable classification in Indonesia using dynamic time warping of Sentinel-1A dual polarization SAR time series," *Int. J. Appl. Earth Observ. Geoinf.*, vol. 2019, pp. 268–280, Feb. 2019, doi: [10.1016/j.jag.2019.01.009](https://doi.org/10.1016/j.jag.2019.01.009).
- [38] Y. Qu, W. Z. Zhao, Z. L. Yuan, and J. G. Chen, "Crop mapping from Sentinel-1 polarimetric time-series with a deep neural network," *Remote Sens.*, vol. 12, no. 15, Aug. 2020, Art. no. 2493, doi: [10.3390/rs12152493](https://doi.org/10.3390/rs12152493).
- [39] G. W. Gella, W. Bijker, and M. Belgiu, "Mapping crop types in complex farming areas using SAR imagery with dynamic time warping," *ISPRS J. Photogramm. Remote Sens.*, vol. 175, pp. 171–183, May 2021, doi: [10.1016/j.isprsjprs.2021.03.004](https://doi.org/10.1016/j.isprsjprs.2021.03.004).
- [40] C. Witharana and D. L. Civco, "Optimizing multi-resolution segmentation scale using empirical methods: Exploring the sensitivity of the supervised discrepancy measure Euclidean distance 2 (ED2)," *ISPRS J. Photogramm. Remote Sens.*, vol. 87, pp. 108–121, Jan. 2014, doi: [10.1016/j.isprsjprs.2013.11.006](https://doi.org/10.1016/j.isprsjprs.2013.11.006).

- [41] S. Deng, L. Du, C. Li, J. Ding, and H. W. Liu, "SAR automatic target recognition based on Euclidean distance restricted autoencoder," *IEEE J. Sel. Topics Appl. Earth Observ. Remote Sens.*, vol. 10, no. 7, pp. 3323–3333, Jul. 2017, doi: [10.1109/jstars.2017.2670083](https://doi.org/10.1109/jstars.2017.2670083).
- [42] O. Csillik, M. Belgiu, G. P. Asner, and M. Kelly, "Object-based time-constrained dynamic time warping classification of crops using Sentinel-2," *Remote Sens.*, vol. 11, no. 10, May 2019, Art. no. 1257, doi: [10.3390/rs11101257](https://doi.org/10.3390/rs11101257).
- [43] S. Moharana, B. Kambhammettu, S. Chintala, A. S. Rani, and R. Avtar, "Spatial distribution of inter- and intra-crop variability using time-weighted dynamic time warping analysis from Sentinel-1 datasets," *Remote Sens. Appl., Soc. Environ.*, vol. 24, Nov. 2021, Art. no. 100630, doi: [10.1016/j.rsase.2021.100630](https://doi.org/10.1016/j.rsase.2021.100630).
- [44] H. Y. Li, J. H. Wan, S. W. Liu, H. Sheng, and M. M. Xu, "Wetland vegetation classification through multi-dimensional feature time series remote sensing images using Mahalanobis distance-based dynamic time warping," *Remote Sens.*, vol. 14, no. 3, Feb. 2022, Art. no. 501, doi: [10.3390/rs14030501](https://doi.org/10.3390/rs14030501).
- [45] X. D. Guan, C. Huang, G. H. Liu, X. L. Meng, and Q. S. Liu, "Mapping rice cropping systems in Vietnam using an NDVI-based time-series similarity measurement based on DTW distance," *Remote Sens.*, vol. 8, no. 1, Jan. 2016, Art. no. 19, doi: [10.3390/rs8010019](https://doi.org/10.3390/rs8010019).
- [46] S. Mondal and C. Jeganathan, "Mountain agriculture extraction from time-series MODIS NDVI using dynamic time warping technique," *Int. J. Remote Sens.*, vol. 39, no. 11, pp. 3679–3704, Dec. 2018, doi: [10.1080/01431161.2018.1444289](https://doi.org/10.1080/01431161.2018.1444289).
- [47] M. Belgiu, Y. Zhou, M. Marshall, and A. Stein, "Dynamic time warping for crops mapping," *Int. Arch. Photogramm., Remote Sens. Spatial Inf. Sci.*, vol. XLIII-B3-2020, pp. 947–951, 2020, doi: [10.5194/isprs-archives-XLIII-B3-2020-947-2020](https://doi.org/10.5194/isprs-archives-XLIII-B3-2020-947-2020).
- [48] M. Vreugdenhil et al., "Sensitivity of Sentinel-1 backscatter to vegetation dynamics: An Austrian case study," *Remote Sens.*, vol. 10, no. 9, Sep. 2018, Art. no. 1369, doi: [10.3390/rs10091396](https://doi.org/10.3390/rs10091396).
- [49] M. Meroni et al., "Comparing land surface phenology of major European crops as derived from SAR and multispectral data of Sentinel-1 and -2," *Remote Sens. Environ.*, vol. 253, Feb. 2021, Art. no. 112232, doi: [10.1016/j.rse.2020.112232](https://doi.org/10.1016/j.rse.2020.112232).



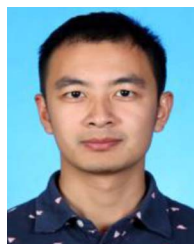
Bingkun Liang (Student Member, IEEE) received the B.S. degree in civil engineering from Hunan Agricultural University, Changsha, China, in 2016, and the M.S. degree in sociology in 2019 from Sun Yat-sen University, Guangzhou, China, where he is currently working toward the Ph.D. degree in geography.

His research interests include crop classification, signal processing, and remote sensing.



Rongkun Zhao received the B.S. degree in geographic information science and the M.S. degree in cartography and geographic information system from Southwest University, Chongqing, China, in 2020 and 2022, respectively. She is currently working toward the Ph.D. degree in microwave remote sensing inversion of rape crop parameters with the Institute of Agricultural Resources and Regional Planning, Chinese Academy of Agricultural Sciences, Beijing, China.

Her major research interests include agricultural remote sensing applications, crop growth monitoring, and critical crop parameter retrieval.



Jieyang Tan received the B.S. degree in land resources management from Hunan Agricultural University, Changsha, China, in 2012, and the M.S. degree in agricultural remote sensing from the Chinese Academy of Agricultural Sciences, Beijing, China, in 2015.

He is currently an Assistant Researcher with the Institute of Agricultural Economics and Agricultural Zoning, Hunan Academy of Agricultural Sciences, Changsha, China. His main research interests are in agricultural remote sensing applications.



Lang Xia received the B.S. degree in land resources management from Inner Mongolia Agricultural University, Hohhot, China, in 2011, and the M.S. degree in rural and regional development from the Chinese Academy of Agricultural Sciences, Beijing, China, in 2015.

His main research interests include deep learning crop mapping models and remote sensing radiation transmission simulation and applications.



Hong Cao received the B.S. degree in geographic information science from Huazhong Agricultural University, Wuhan, China, in 2022. She is currently working toward the M.S. degree in agricultural remote sensing with the Chinese Academy of Agricultural Sciences, Beijing, China.

Her main research interests are in remote sensing data assimilation for crop yield estimation.



Shangrong Wu (Member, IEEE) received the B.S. degree in information countermeasure technology from Xidian University, Xi'an, China, in 2010, the M.S. degree in signal and information processing from North University of China, Taiyuan, China, in 2013, and the Ph.D. degree in agricultural remote sensing from the Chinese Academy of Agricultural Sciences, Beijing, China, in 2019.

She is currently an Associate Researcher with the Institute of Agricultural Resources and Regional Planning, Chinese Academy of Agricultural Sciences. Her research interests include the application of agricultural remote sensing, crop growth monitoring, crop yield simulation and forecasting, critical crop parameter retrieval, and data assimilation.



Peng Yang received the B.S. degree in environmental science from Wuhan University, Hubei, China, in 1996, the M.Eng. degree in environmental engineering from the Chinese Academy of Agricultural Sciences, Beijing, China, in 2000, and the Ph.D. degree in civil engineering from the University of Tokyo, Tokyo, Japan, in 2005.

He is currently a Research Professor with the Institute of Agricultural Resources and Regional Planning, Chinese Academy of Agricultural Sciences. His research interests include the impacts of climate change on agriculture and food security in China. He has been involved in many national projects related to the impact assessment of climate change on food security and monitoring and modeling of cropping systems and crop areas by using remote sensing and GIS.